



Hollow zeolite-encapsulated Fe-Cu bimetallic catalysts for phenol degradation



Chengyi Dai^{a,b}, Anfeng Zhang^b, Lei Luo^b, Xinbao Zhang^b, Min Liu^b, Junhu Wang^c, Xinwen Guo^{b,*}, Chunshan Song^{b,d,**}

^a School of Chemical Engineering, Northwest University, Xi'an 710069, China

^b State Key Laboratory of Fine Chemicals, PSU-DUT Joint Center for Energy Research, School of Chemical Engineering, Dalian University of Technology, Dalian 116024, China

^c Mossbauer Effect Data Center, Dalian Institute of Chemical Physics, Chinese Academy of Sciences, Dalian 116023, China

^d EMS Energy Institute, PSU-DUT Joint Center for Energy Research, Department of Energy & Mineral Engineering, Department of Chemical Engineering, Pennsylvania State University, University Park, PA 16802, United States

ARTICLE INFO

Article history:

Received 3 October 2016

Received in revised form 21 January 2017

Accepted 1 February 2017

Available online 7 February 2017

Keywords:

Hollow zeolite

Phenol degradation

Fe-Cu bimetal

Encapsulate

ABSTRACT

Highly dispersed Fe-Cu bimetallic oxide nanoparticles were successfully encapsulated in hollow Silicalite-1 single crystals ($\text{Fe}_2\text{O}_3-\text{CuO}@\text{Hol S-1}$) by tetrapropylammonium hydroxide (TPAOH) hydrothermal treatment with an “impregnation-dissolution-recrystallization” process. Due to the Fe-Cu bimetallic interaction compared with single iron oxide, Fe-Cu bimetallic oxide exhibits a higher dispersion with the particle size decreasing from ~11.3 nm to ~3.7 nm. For aqueous phenol degradation, the $\text{Fe}_2\text{O}_3-\text{CuO}@\text{Hol S-1}$ catalyst exhibits high activity attributed to the enhanced transport of reactants/products in the short microporous channels (20 nm) and the small metal oxide particle size. Interestingly, the particle size of encapsulated $\text{Fe}_2\text{O}_3-\text{CuO}$ (3.7 nm) is larger than that of zeolite micropore (0.53 nm), which helps preventing the leaching of metal oxide that is a significant problem for conventional supported Fe catalyst in this reaction.

© 2017 Elsevier B.V. All rights reserved.

1. Introduction

Fenton-type oxidation has attracted great attention as an advanced oxidation process for degradation of environmental pollutants such as phenol [1–6]. Application of Fenton reaction for phenolic wastewater treatment with hydrogen peroxide is mostly based on homogeneous catalysis by metal ions (Fe^{2+} and others) in aqueous solution [7]. However, the optimum pH value range of Fenton-type oxidation is narrow (near pH 3) for high-efficiency oxidation by Fenton's reagent. On the other hand, the use of metallic salts as catalysts induces an additional pollution. In recent years, many kinds of heterogeneous catalysts have been investigated for phenol degradation under near neutral conditions [1,8,9]. Among these heterogeneous catalysts, iron (Fe)-based catalysts are more

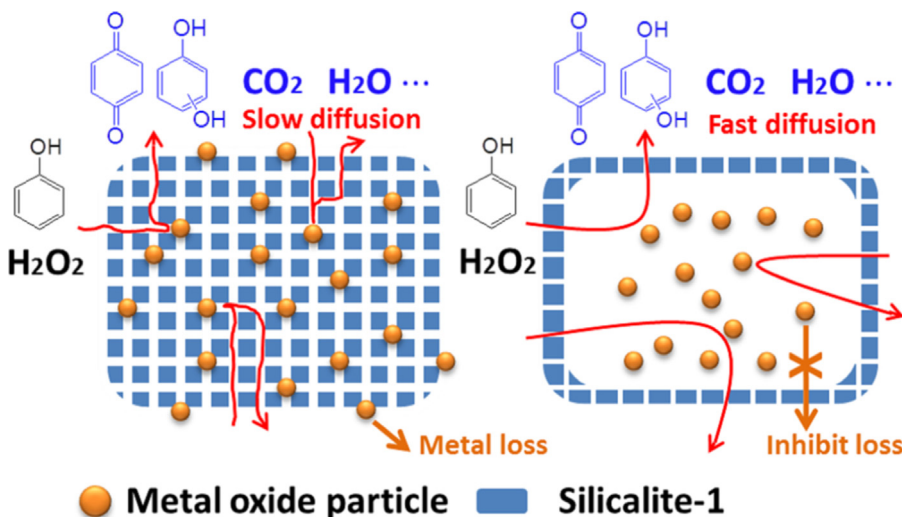
promising because of their high activity, low cost and extensive supply [10,11]. Compared with homogeneous Fe catalysts, a drawback of heterogeneous Fe catalysts is the lower accessibility of the active metal sites. To solve this problem, Fe oxide particles were usually supported on the porous materials, such as mesoporous silica [12,13] and mesoporous carbon [14]. In addition, because the reaction takes place on the surface of the metal oxide, increasing the surface of metal oxide or reducing its particle size can also effectively increase the contact between the active metal sites and the reactants [15,16]. On the other hand, by introducing other elements such as Cu [17], Mn [18], Co [19], V [20], Ti [21] and Cr [22] into the Fe catalyst, it is possible to effectively adjust the physicochemical properties of Fe, increase the activity of the catalyst. However, for heterogeneous Fenton catalysts, there are still challenges regarding how to improve the metal dispersion and how to prevent metal loss.

Zeolites as metal supports have attracted interest due to their high hydrothermal stability, uniform micropores, and unique shape selectivity which can be applied in catalytic operations [23–27]. However, in conventional zeolites, the long and narrow pore channels limit the diffusion of reactants and products [28], especially

* Corresponding author.

** Corresponding author at: EMS Energy Institute, PSU-DUT Joint Center for Energy Research, Department of Energy & Mineral Engineering, Department of Chemical Engineering, Pennsylvania State University, University Park, PA, 16802, United States.

E-mail addresses: guoxw@dlut.edu.cn (X. Guo), csong@psu.edu (C. Song).



Scheme 1. Schematic drawing of the phenol degradation on the Fe-based catalysts.

in the liquid phase, which inhibits the accessibility of reactants to metals. On the other hand, the metal particles are compactly stuck in the zeolite that reduces the exposed surface of the metal and further slow the diffusion of reactants and products. These factors limit the application of metal-supported zeolite in the liquid phase reaction [29]. Use mesoporous zeolite as metal support is a commonly method to break the above limitation. In our recent work, Fe-Cu bimetallic oxides have been supported on mesoporous ZSM-5 zeolite [30]. The rough mesoporous surface of support sufficiently enhanced the dispersion and prohibited metal migration, therefore enhancing the bimetallic interaction, and promoting catalytic oxidation of phenol. However, the open pore system also promotes the loss of metal during the reaction, resulting in high content of iron and copper, greater than 1 ppm, in the product solution. Encapsulate Fe-Cu bimetallic oxides in hollow zeolite, ensuring high dispersion of the metal oxide and short channel in the zeolite wall, maybe a better solution (**Scheme 1**). However, according to previous studies, it remains a great challenge to synthesis metal-encapsulated hollow zeolite to meet the above requirements, such as the metal particles usually can't completely encapsulate in the cavity and/or they usually agglomerate in the cavity of hollow zeolite during encapsulation process [31–33], which limit the performance of the sample.

In this report, we propose an effective approach involving highly dispersed Fe-Cu bimetallic oxide particles encapsulated into the hollow Silicalite-1 (Hol S-1) crystal using suitable precursor salts. As expected, the activity of metal can be effectively improved when encapsulated in the interior of hollow zeolite for the liquid phase reaction. For aqueous phenol degradation, the catalytic activity of Fe oxide and Fe-Cu bimetallic oxide encapsulated in Hol S-1 was found to be about 7.5 and 20 times higher than that of Fe oxide supported on conventional nano-S-1 zeolite, respectively. The excellent activity is benefited from the high dispersion of metal oxide nanoparticles, the strong Fe-Cu bimetallic interaction and the short channels in the hollow zeolite wall. Interestingly, the hollow crystal wall with micropores prevents the leaching of encapsulated metal oxide, enhancing the catalyst reusability.

The present work provides a general and robust strategy to prepare multi-metallic catalysts with well-dispersed nanoparticles with high activity and reusability for the reaction of phenol degradation. For the recent research on the photocatalytic degradation of organic pollutants [34–37], the encapsulation strategy also has potential applications for the design and synthesis of bimetallic photocatalytic materials.

2. Experimental

2.1. Preparation of silicalite-1 zeolite

Silicalite-1 (S-1) was synthesized with the clear solution method. Typically, 15.4 ml of tetraethyl orthosilicate (TEOS) was mixed with a certain amount of tetrapropylammonium hydroxide (TPAOH) solution. The molar composition of the synthesis mixture was 1 TEOS: 0.27 TPAOH: 37 H₂O. After being stirred for 3 h at 35 °C, the solution was heated at 80 °C to remove the ethanol generated during the hydrolysis of TEOS and then water was added to maintain constant volume. After crystallization at 170 °C for 3 days, the product was recovered by centrifugation and dried overnight at 100 °C. Finally, the template was removed by calcination in static air at 540 °C for 6 h.

2.2. Preparation of $\text{Fe}_2\text{O}_3@\text{Hol S-1}$, $\text{CuO}@\text{Hol S-1}$ and $\text{Fe}_2\text{O}_3-\text{CuO}@\text{Hol S-1}$

$\text{Fe}_2\text{O}_3/\text{S-1}$ was synthesized by an incipient-wetness impregnation method. In brief, the calcined Silicalite-1 was impregnated with an aqueous solution of FeCl_3 ; after drying overnight at 100 °C, the product was calcined in static air at 500 °C for 4 h. The ideal Fe loading on the $\text{Fe}_2\text{O}_3/\text{S-1}$ was 0.72 mmol/g.

The as-prepared $\text{Fe}_2\text{O}_3/\text{S-1}$ was treated with 0.3 M TPAOH (20 ml of solution per gram of zeolite) at 170 °C for 72 h, then dried overnight at 100 °C and calcined in static air at 500 °C for 4 h to obtain $\text{Fe}_2\text{O}_3@\text{Hol S-1}$.

$\text{CuO}/\text{S-1}$ was prepared by the same method as $\text{Fe}_2\text{O}_3/\text{S-1}$, using CuCl_2 as the copper (Cu) source. The ideal Cu loading on $\text{Cu}/\text{S-1}$ was 0.72 mmol/g. After treatment with 0.3 M TPAOH (20 ml of solution per gram of zeolite) at 170 °C for 72 h, drying overnight at 100 °C and calcining in static air at 500 °C for 4 h, the $\text{CuO}@\text{Hol S-1}$ was obtained.

Bimetals encapsulated in the hollow S-1 were prepared by similar methods as the single metals. FeCl_3 and CuCl_2 were used as the Fe and Cu sources, respectively, and a co-impregnation method was used to synthesize bimetals/S-1. The ideal Fe loading on the S-1 was 0.48 mmol/g, while the ideal Cu loading on the S-1 was 0.24 mmol/g. The as-prepared $\text{Fe}_2\text{O}_3-\text{CuO}/\text{S-1}$ was treated with 0.3 M TPAOH (20 ml of solution per gram of zeolite) at 170 °C for 72 h, then dried overnight at 100 °C and calcined in static air at 500 °C for 4 h to obtain $\text{Fe}_2\text{O}_3-\text{CuO}@\text{Hol S-1}$.

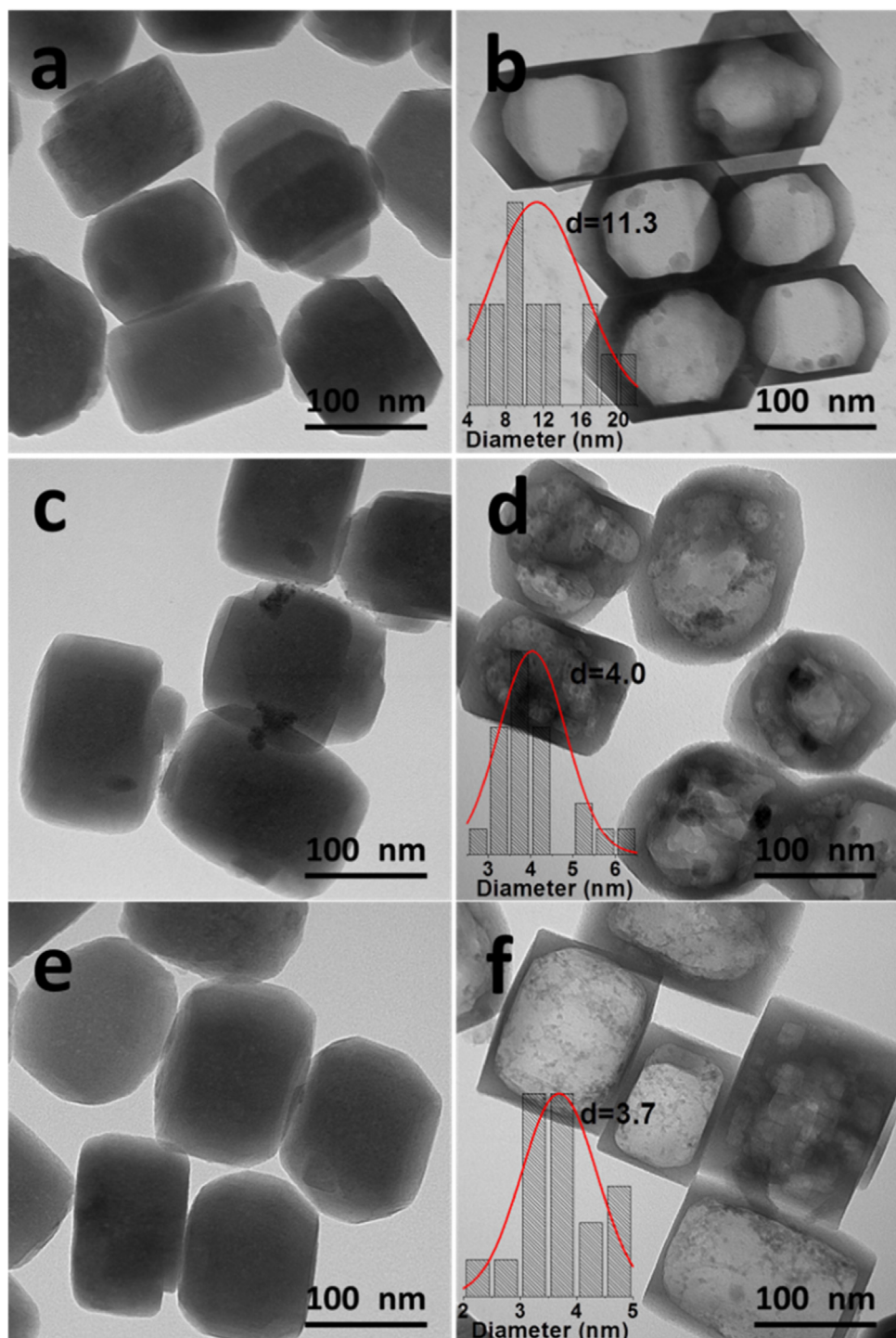


Fig. 1. TEM images of (a) $\text{Fe}_2\text{O}_3/\text{S}-1$, (b) $\text{Fe}_2\text{O}_3@\text{Hol S}-1$, (c) $\text{CuO}/\text{S}-1$, (d) $\text{CuO}@\text{Hol S}-1$, (e) $\text{Fe}_2\text{O}_3-\text{CuO}/\text{S}-1$, (f) $\text{Fe}_2\text{O}_3-\text{CuO}@\text{Hol S}-1$.

The real Fe and Cu loadings on the samples are listed in Table 1, as measured by inductively coupled plasma (ICP) mass spectrometry.

As compared, $\text{Fe}_2\text{O}_3/\text{S}-1$, $\text{Fe}_2\text{O}_3@\text{Hol S}-1$, $\text{CuO}/\text{S}-1$, $\text{CuO}@\text{Hol S}-1$, $\text{Fe}_2\text{O}_3-\text{CuO}/\text{S}-1$ and $\text{Fe}_2\text{O}_3-\text{CuO}@\text{Hol S}-1$ were prepared using the same method and select ferric nitrate and Cu nitrate as Fe and Cu source, respectively. (Fig. 2) The resulting samples were denoted as $\text{Fe}_2\text{O}_3/\text{S}-1(\text{nitrate})$, $\text{Fe}_2\text{O}_3@\text{Hol S}-1(\text{nitrate})$, $\text{CuO}/\text{S}-1(\text{nitrate})$, $\text{CuO}@\text{Hol S}-1(\text{nitrate})$, $\text{Fe}_2\text{O}_3-\text{CuO}/\text{S}-1(\text{nitrate})$ and $\text{Fe}_2\text{O}_3-\text{CuO}@\text{Hol S}-1(\text{nitrate})$, respectively.

2.3. Characterization

Powder X-ray diffraction (XRD) patterns were recorded on a Rigaku Smartlab diffractometer using a nickel-filtered $\text{CuK}\alpha$ X-ray source at a scanning rate of 0.02° over the range between 5° and 80° .

Transmission electron microscopy (TEM) images were taken on a Tecnai G2 20 S-twin instrument (FEI Company) with an acceleration voltage of 200 kV. The samples for TEM analysis were prepared by dipping the carbon-coated copper grids into the ethanol solutions of the samples and drying at ambient condition.

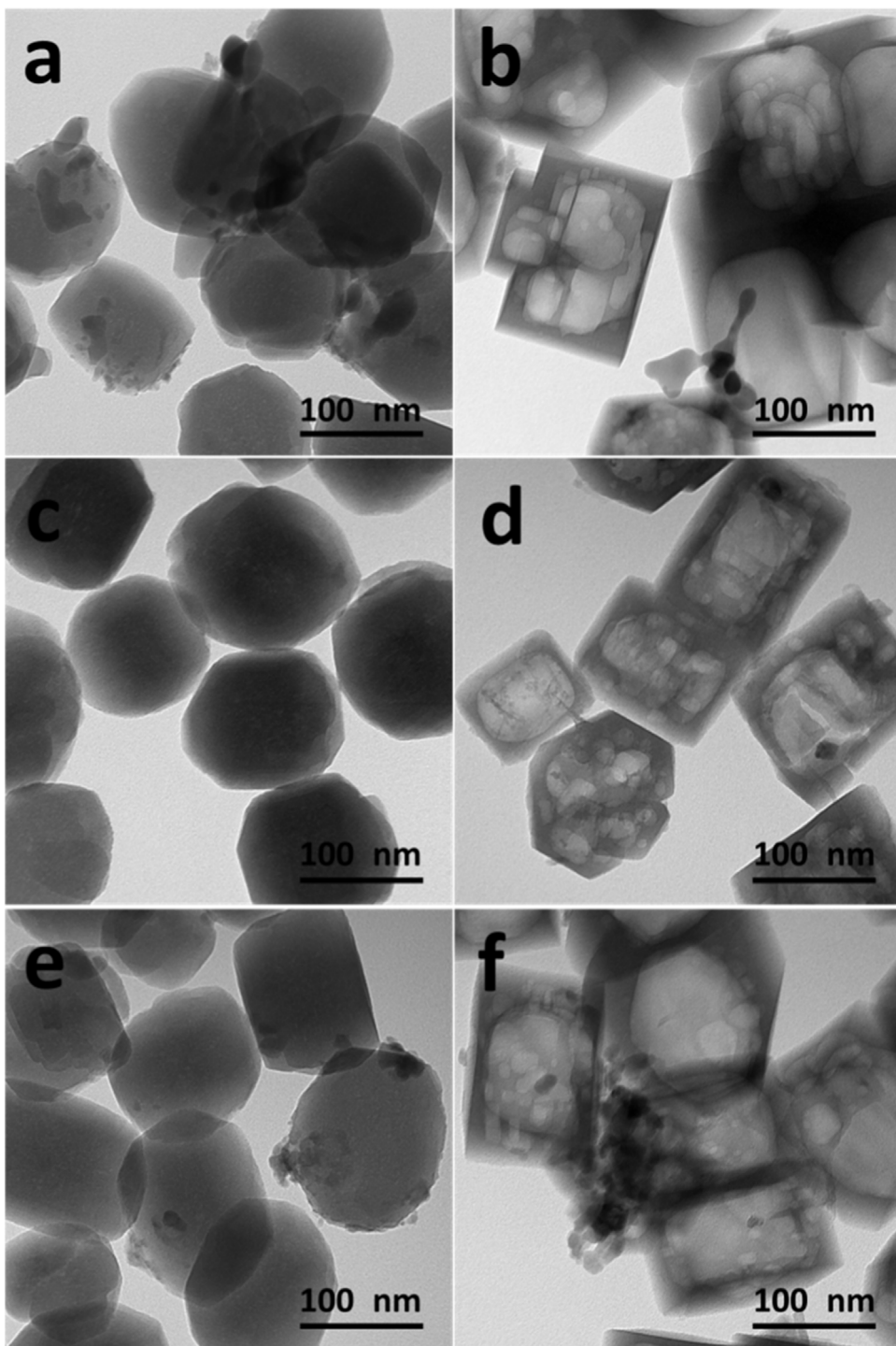


Fig. 2. TEM images of (a) $\text{Fe}_2\text{O}_3/\text{S}-1(\text{nitrate})$, (b) $\text{Fe}_2\text{O}_3@\text{Hol S}-1(\text{nitrate})$, (c) $\text{CuO}/\text{S}-1(\text{nitrate})$, (d) $\text{CuO}@\text{Hol S}-1(\text{nitrate})$, (e) $\text{Fe}_2\text{O}_3-\text{CuO}/\text{S}-1(\text{nitrate})$, (f) $\text{Fe}_2\text{O}_3-\text{CuO}@\text{Hol S}-1(\text{nitrate})$.

Ar isotherms were measured with a Quantachrome autosorb-iQ2 gas adsorption analyzer at -186°C . Prior to the measurement, the samples were degassed in vacuum at 300°C for 10 h. The Brunauer-Emmett-Teller (BET) method was applied to calculate the total surface area (S_{BET}), while the t-plot method was used to discriminate between micro- and mesoporosity. In the t-plot, the reported mesopore surface area (S_{meso}) consists of contributions from the outer surface of the particles as well as mesopores and macropores.

The elemental analysis of catalysts was carried out on a Perkin Elmer OPTIMA 2000DV ICP Optical Emission Spectrometer.

H_2 -TPR measurements were carried out with a ChemBET Pulsar TPR/TPD instrument (Quantachrome, USA) to analyze the reducibility of the calcined catalysts. Prior to the reduction, the calcined sample (0.10 g) was placed in a quartz tube reactor in the interior of a controlled oven. The sample was flushed with high purity argon at 300°C for 1 h to remove water and other contaminants then cooled to room temperature. A gas mixture containing 5 vol% H_2 in Ar was passed through the sample at a total flow rate of 30 ml min^{-1} . The

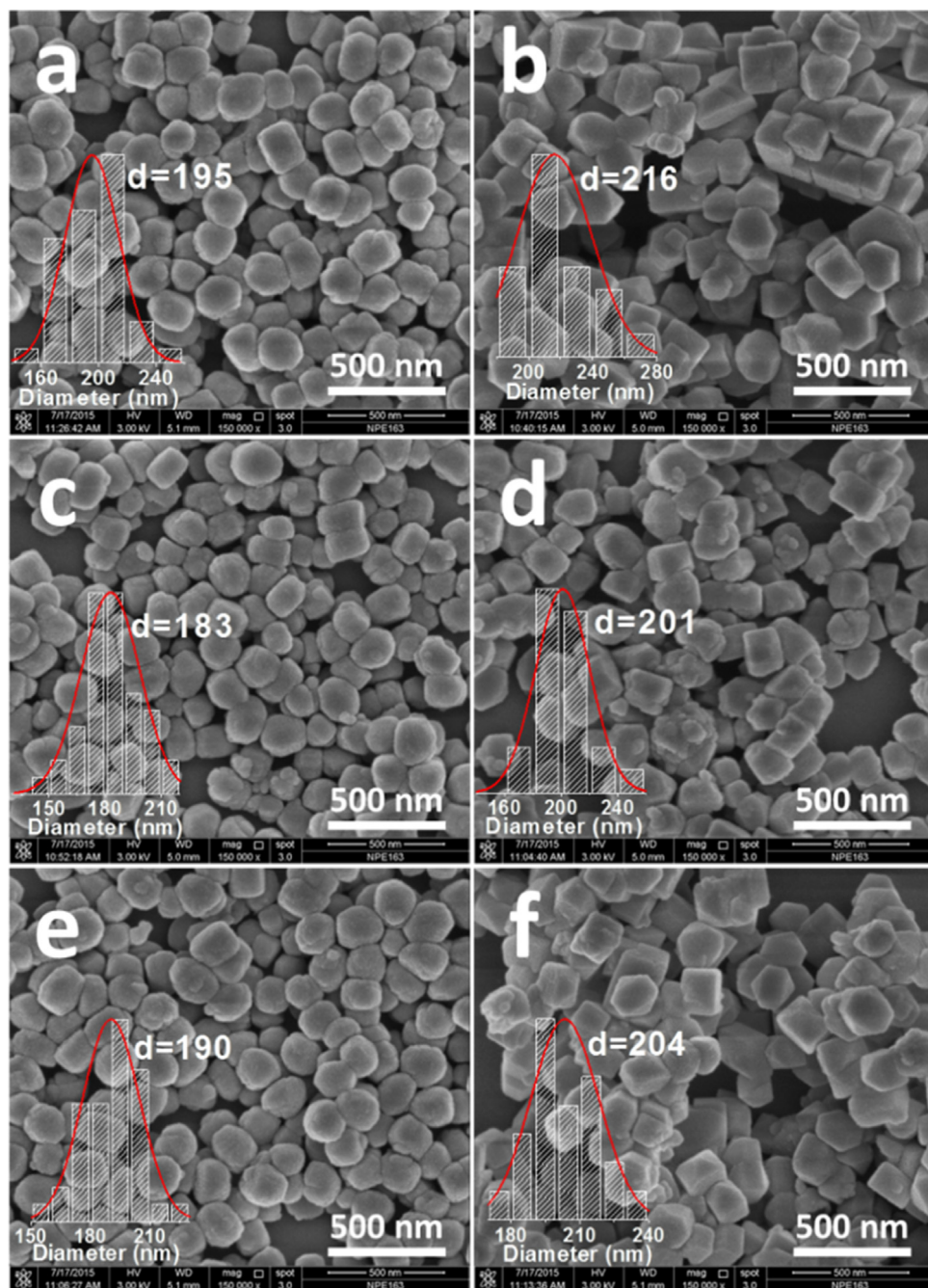


Fig. 3. SEM images of (a) $\text{Fe}_2\text{O}_3/\text{S}-1$, (b) $\text{Fe}_2\text{O}_3@\text{Hol S-1}$, (c) CuO/S-1 , (d) $\text{CuO}@\text{Hol S-1}$, (e) $\text{Fe}_2\text{O}_3-\text{CuO/S-1}$, (f) $\text{Fe}_2\text{O}_3-\text{CuO}@\text{Hol S-1}$.

Table 1

Textural properties of $\text{Fe}_2\text{O}_3/\text{S}-1$, $\text{Fe}_2\text{O}_3@\text{Hol S-1}$, CuO/S-1 , $\text{CuO}@\text{Hol S-1}$, $\text{Fe}_2\text{O}_3-\text{CuO/S-1}$ and $\text{Fe}_2\text{O}_3-\text{CuO}@\text{Hol S-1}$.

Sample Code	Yield [%]	Fe ^a [mmol/g]	Cu ^a [mmol/g]	$S_{\text{micro}}^{\text{b}}$ [$\text{m}^2 \text{g}^{-1}$]	$S_{\text{meso}}^{\text{b}}$ [$\text{m}^2 \text{g}^{-1}$]	$S_{\text{BET}}^{\text{c}}$ [$\text{m}^2 \text{g}^{-1}$]	$V_{\text{micro}}^{\text{b}}$ [$\text{cm}^3 \text{g}^{-1}$]	$V_{\text{pore}}^{\text{d}}$ [$\text{cm}^3 \text{g}^{-1}$]
$\text{Fe}_2\text{O}_3/\text{S}-1$	–	0.72	–	332	110	442	0.13	0.43
$\text{Fe}_2\text{O}_3@\text{Hol S-1}$	83	0.87	–	317	127	444	0.12	0.68
CuO/S-1	–	–	0.57	326	115	441	0.13	0.47
$\text{CuO}@\text{Hol S-1}$	85	–	0.51	204	167	371	0.08	0.60
$\text{Fe}_2\text{O}_3-\text{CuO/S-1}$	–	0.51	0.17	357	125	482	0.14	0.49
$\text{Fe}_2\text{O}_3-\text{CuO}@\text{Hol S-1}$	84	0.60	0.19	296	146	442	0.12	0.87

^a ICP method.

^b t-plot method.

^c BET method.

^d $p/p_0 = 0.99$.

temperature and detector signals were then continuously recorded while heating at $10^{\circ}\text{C min}^{-1}$ up to 900°C . A cooling trap was also placed between the sample and the detector for removal of released water formed during the reduction process.

2.4. Catalytic tests

The degradation of phenol in aqueous solution was performed in a stirred glass reactor. The reaction conditions were as follows: the reaction temperature 50°C , atmospheric pressure; 50 ml of aqueous solution of 1.0 g phenol/L; the catalyst weight was of 0.1 g; the molar ratio of $\text{H}_2\text{O}_2/\text{phenol}$ was 14, and initial solution pH 6.2. The concentration of phenol and other reaction products was determined by liquid chromatography (HPLC, Agilent 1200). The conversion of phenol X (phenol) was calculated as follows:

$$X(\text{phenol}) = (1 - C_t/C_0) \times 100\% \quad (1)$$

The C_0 and C_t stand for the phenol concentration at the initial time and at time t, respectively.

3. Results and discussion

Fig. 1a shows a TEM image of prepared $\text{Fe}_2\text{O}_3/\text{S}-1$ after calcination at 500°C for 4 h. Fe_2O_3 nanoparticles are highly dispersed on the ZSM-5 crystals, no significant presence of large Fe_2O_3 particles was observed. When the ferric nitrate was used as Fe source, large Fe_2O_3 particles with about 20 nm were located on the surface of the crystals (**Fig. 2a**). The difference in particle size may be attributed to the different melting points of Fe sources as well as their various interactions with supports. For FeCl_3 , its melting point, ca. 306°C , is higher than drying temperature, it maintains a high degree of dispersion during drying. When $\text{Fe}(\text{NO}_3)_3$ was used as Fe source, during the drying process, it transformed into a liquid-like state because of its low melting point, ca. 47°C . After TPAOH treatment, large voids were formed in the Silicalite-1 crystals by controlled silicon leaching with OH^- and thin, intact shells were formed by the re-crystallization of silicon on the crystal surface with TPA^+ . The thickness of shell was only about 20 nm, which enhances the diffusion of reactants and products in the micropores. In this process, Fe oxide species in the micropores on the crystal surfaces become encapsulated in the voids of hollow crystals (**Fig. 1b**). However, large Fe oxide particles fall down from the surface during the “dissolution-recrystallization” process and remain on the hollow crystal surfaces (**Fig. 2b**). In the case of Fe oxide encapsulated in the voids of hollow crystals (**Fig. 1b**), the Fe_2O_3 particles grew larger to about 11.3 nm during TPAOH treatment process under 170°C and the subsequent calcination at 500°C .

Figs. 1 c and 2 c show typical TEM images of the prepared $\text{CuO}/\text{S}-1$. When CuCl_2 was used as Cu source whose melting point is about 100°C , same as the drying temperature, a small amount of Cu oxide particles were located on the crystal surface after calcination (**Fig. 1c**). When $\text{Cu}(\text{NO}_3)_2$ was used as Cu source whose melting point increases to about 115°C , the Cu oxide dispersion of $\text{CuO}/\text{S}-1$ (nitrate) is higher than that of $\text{CuO}/\text{S}-1$ (**Fig. 2c**). After TPAOH treatment, most Cu oxide particles were encapsulated in the hollow crystals for both samples. However, as expected, the Cu oxide dispersion in the $\text{CuO}@/\text{Hol S}-1$ is lower than $\text{CuO}@/\text{Hol S}-1$ (nitrate), showing more large particles in the hollow crystals.

Fig. 1e shows a typical TEM image of the prepared $\text{Fe}_2\text{O}_3-\text{CuO}/\text{S}-1$. Contrary to sample of $\text{CuO}/\text{S}-1$, there are no observable particles on the surface of crystals. This is attributed to a high dispersion of Fe and Cu. After TPAOH treatment, several particles with average size of 3.7 nm were encapsulated in the hollow crystals (**Fig. 1f**). These $\text{Fe}_2\text{O}_3-\text{CuO}$ particles are smaller than the encapsulated monometallic Fe_2O_3 and CuO particles (**Fig. 1b** and d). These results confirm that the presence of Fe and Cu together significantly

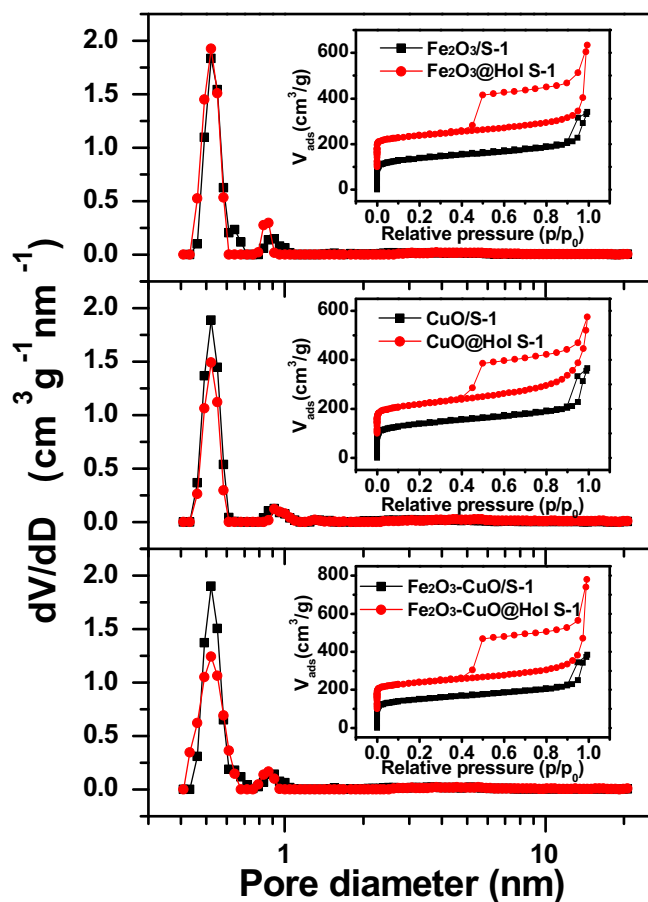


Fig. 4. Ar adsorption and desorption isotherms at 87 K (inset) and pore size distributions of $\text{Fe}_2\text{O}_3/\text{S}-1$, $\text{Fe}_2\text{O}_3@/\text{Hol S}-1$, $\text{CuO}/\text{S}-1$, $\text{CuO}@/\text{Hol S}-1$, $\text{Fe}_2\text{O}_3-\text{CuO}/\text{S}-1$ and $\text{Fe}_2\text{O}_3-\text{CuO}@/\text{Hol S}-1$. The isotherms of hollow samples are offset by $100\text{ cm}^3\text{ g}^{-1}$. The pore size distributions were determined by non-local density functional theory (NLDFT).

inhibited aggregation of metal particles during TPAOH treatment process. In the case of $\text{Fe}_2\text{O}_3-\text{CuO}/\text{S}-1$ (nitrate), the addition of Cu could also improve the dispersion of Fe oxide (**Fig. 2e**). However, after TPAOH treatment, most of bimetallic particles remain on the hollow crystal surfaces (**Fig. 2f**).

Fig. 3 shows the SEM images of the six catalysts with the inset giving the particle size distribution. The parent Silicalite-1 shows a uniform particle size distribution around 183–195 nm. After alkaline treatment, the morphologies of nanocubes are more regular, the sizes are larger than the parent samples, ca. 201–216 nm, and their shells were not damaged, which demonstrate the re-crystallization occurs at the outer surface of Silicalite-1 crystals.

Fig. 4 shows Ar adsorption and desorption isotherms at -186°C (inset) and pore size distributions of the samples. The Ar adsorption-desorption isotherms of metal-encapsulated hollow crystals show an H2 hysteresis loop with an abrupt step around $p/p_0 = 0.45$ in the desorption branch. This shows that, during the TPAOH treatment, the hollow structure of the zeolite is preserved, which is consistent with the TEM and SEM results. The micropore size distributions derived from the Ar adsorption isotherms indeed confirm that the original micropore size is not affected during the alkaline treatment. **Table 1** lists textual properties of the samples. Compared with solid crystals, the micropore surface areas and volumes of the hollow crystals decrease after TPAOH treatment, while the mesopore surface areas and total pore volumes increase.

Fig. 5 shows the XRD patterns of the samples, the five characteristic diffraction peaks at 7.8° , 8.8° , 23.0° , 23.9° and 24.4° are

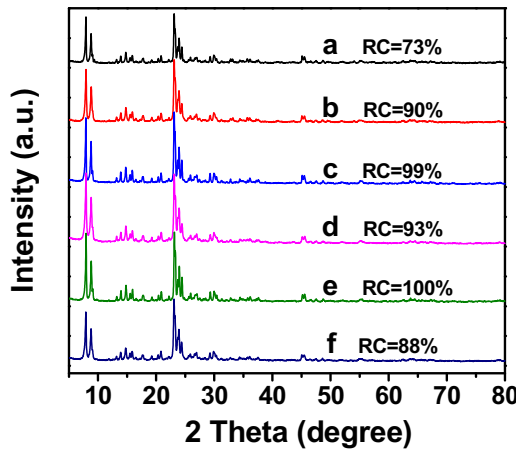


Fig. 5. XRD patterns of (a) $\text{Fe}_2\text{O}_3/\text{S}-1$, (b) $\text{Fe}_2\text{O}_3@\text{Hol S}-1$, (c) $\text{CuO}/\text{S}-1$, (d) $\text{CuO}@\text{Hol S}-1$, (e) $\text{Fe}_2\text{O}_3-\text{CuO}/\text{S}-1$, (f) $\text{Fe}_2\text{O}_3-\text{CuO}@\text{Hol S}-1$, 2 theta range from 5 to 80°.

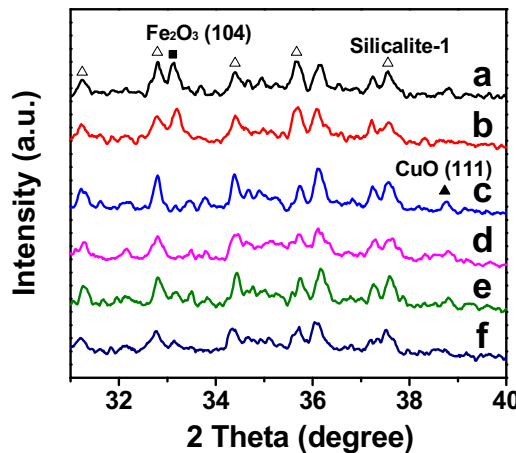


Fig. 6. XRD patterns of (a) $\text{Fe}_2\text{O}_3/\text{S}-1$, (b) $\text{Fe}_2\text{O}_3@\text{Hol S}-1$, (c) $\text{CuO}/\text{S}-1$, (d) $\text{CuO}@\text{Hol S}-1$, (e) $\text{Fe}_2\text{O}_3-\text{CuO}/\text{S}-1$, (f) $\text{Fe}_2\text{O}_3-\text{CuO}@\text{Hol S}-1$, 2 theta range from 31 to 40°.

assigned to those of Silicalite-1 consistently, confirming the MFI structure of the shell. The relative crystallinity (RC) was calculated by comparing the total intensity of the five characteristic peaks with that of each sample and chose the highest total intensity as 100%. Due to the occurrence of recrystallization, both the yield and RC of the samples after TPAOH treatment were higher than 80% (Table 1, Fig. 5). The high dispersion of $\text{Fe}_2\text{O}_3-\text{CuO}$ bimetallics in hollow crystals is also demonstrated by the XRD patterns. Besides the strong diffraction peaks of MFI topology, several new peaks appear between 31° and 40°. As shown in Fig. 6, samples $\text{Fe}_2\text{O}_3/\text{S}-1$ and $\text{Fe}_2\text{O}_3@\text{Hol S}-1$ exhibit α - Fe_2O_3 (JCPDS: 33-0664) diffraction peaks at 33.1°. However, the diffraction peak of α - Fe_2O_3 in the $\text{Fe}_2\text{O}_3-\text{CuO}@\text{Hol S}-1$ became broad, which suggests the particles in the hollow crystals to be smaller. XRD results are consistent with the TEM results.

To further investigate the metal oxide species, the ^{57}Fe Mössbauer spectra of sample $\text{Fe}_2\text{O}_3@\text{Hol S}-1$ and $\text{Fe}_2\text{O}_3-\text{CuO}@\text{Hol S}-1$ are shown in Fig. 7, with the hyperfine interaction parameters summarized in Table 2. The peak type can reflect the particle size by determining whether the Fe oxide particle is super paramagnetic or not. When the particle size of the Fe oxide is above a critical point, super paramagnetic phenomenon converts the peak to a sextet. In contrast, below the critical point the peak presents as a doublet [38,39]. In the case of sample $\text{Fe}_2\text{O}_3@\text{Hol S}-1$, the Mössbauer peaks of IS about 0.36 mm/s and QS about -0.22 mm/s are in agreement with those values for alpha- Fe_2O_3 in the form of sextet, and the

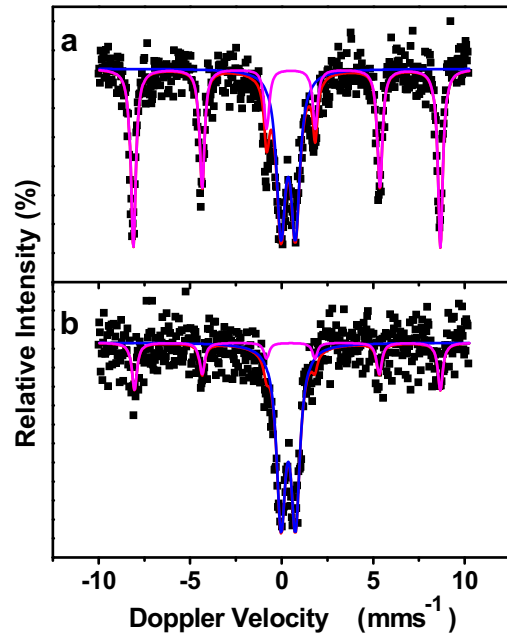


Fig. 7. ^{57}Fe Mössbauer spectra of (a) $\text{Fe}_2\text{O}_3@\text{Hol S}-1$, (b) $\text{Fe}_2\text{O}_3-\text{CuO}@\text{Hol S}-1$ samples at room temperature.

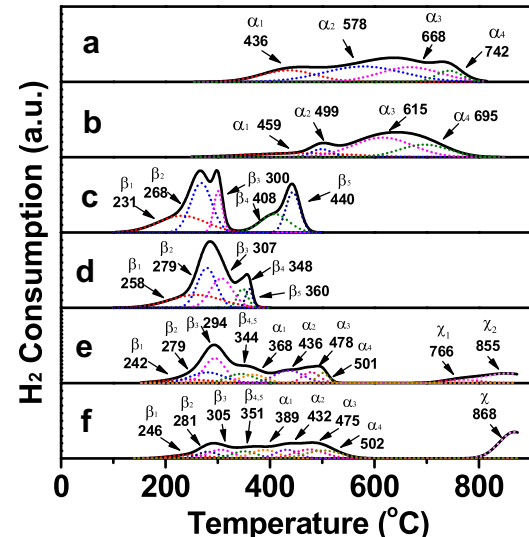


Fig. 8. H₂-TPR profiles of (a) $\text{Fe}_2\text{O}_3/\text{S}-1$, (b) $\text{Fe}_2\text{O}_3@\text{Hol S}-1$, (c) $\text{CuO}/\text{S}-1$, (d) $\text{CuO}@\text{Hol S}-1$, (e) $\text{Fe}_2\text{O}_3-\text{CuO}/\text{S}-1$, (f) $\text{Fe}_2\text{O}_3-\text{CuO}@\text{Hol S}-1$.

peaks of IS about 0.32 mm/s and QS about 0.79 mm/s are in agreement with those values for alpha- Fe_2O_3 in the form of doublet. For sample $\text{Fe}_2\text{O}_3-\text{CuO}@\text{Hol S}-1$, compared with $\text{Fe}_2\text{O}_3@\text{Hol S}-1$, the sextet relative intensity (RI) decreased from 56.6% to 24.5%; simultaneously, the doublet RI increased from 43.4% to 75.5%. This change from sextet to doublet is due to the decrease in particle size, which has been confirmed by TEM and XRD. This also indicates that the introduction of Cu did have a positive impact on minimizing the particle size of Fe oxide.

To gain a better understanding of the interaction between Fe, Cu and support, H₂-TPR experiments were conducted. Fig. 8 shows the H₂-TPR profiles of the samples. For the Fe-containing samples, the four H₂ consumption peaks are attributed to Fe^{3+} and Fe_2O_3 to $\text{Fe}^{(3-d)^+}$ (α_1), with intermediate valence as that in Fe_3O_4 , and then further reduction to Fe^{2+} (α_2). At higher temperature, the peaks represent reduction of Fe^{2+} to Fe^0 (α_3 , α_4) [40,41]. For the Cu-

Table 2

⁵⁷Fe Mössbauer parameters of Fe₂O₃@Hol S-1 and Fe₂O₃—CuO@Hol S-1 samples.

Sample	Oxidation state	Sub-spectrum	IS (mm/s)	QS (mm/s)	Magnetic Field (T)	RI (%)
Fe ₂ O ₃ @Hol S-1	Fe ³⁺	Mixed M + Q	0.36	-0.22	52.0	56.6
	Fe ³⁺	doublet	0.32	0.79	/	43.4
Fe ₂ O ₃ —CuO@Hol S-1	Fe ³⁺	Mixed M + Q	0.36	-0.18	51.8	24.5
	Fe ³⁺	doublet	0.32	0.79	/	75.5

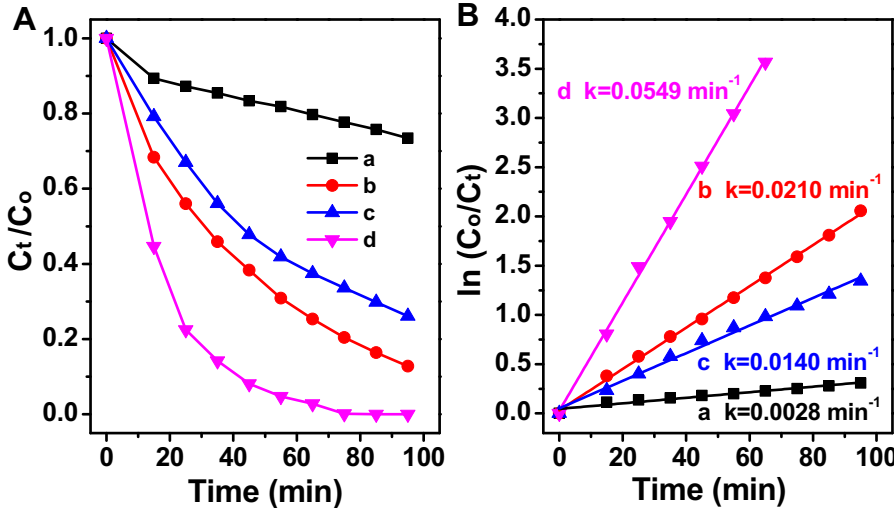


Fig. 9. (A) Phenol degradation and (B) kinetic constant (min^{-1}) catalyzed by (a) Fe₂O₃/S-1, (b) Fe₂O₃@Hol S-1, (c) Fe₂O₃—CuO/S-1 and (d) Fe₂O₃—CuO@Hol S-1, the C₀ and C_t stand for the phenol concentration at the initial time and at time t, respectively. Reaction conditions: molar ratio, 14H₂O₂: 1 phenol, 0.1 g catalyst, 50 ml phenol (1 g/L), temperature is 50 °C, and initial solution pH 6.2.

containing samples, the H₂ consumption peaks are attributed to Cu²⁺ and CuO reduction to Cu⁺ and Cu₂O, then to Cu⁺ reduction to Cu⁰. As the Cu species have a great variety of peaks, we labeled the Cu peaks as β₁, β₂, β₃, β₄, and β₅. According to the H₂-TPR profiles of the catalysts, compare with Fe₂O₃/S-1, the low temperature reduction peak of Fe₂O₃@Hol S-1 moves to higher temperature (Figs. 8a and b 436–459 °C), whereas the high temperature reduction peak of this sample moves to lower temperature (742–695 °C). Similar results also can be found from the Cu loaded samples (Fig. 8c and d). These results confirm that the physicochemical properties of the metals tend to be consistent after TPAOH treatment. That is because the metal species on the crystal surface and in the micropores show different physicochemical properties before TPAOH treatment. After TPAOH treatment, most metal oxide particles were encapsulated in the hollow crystal cavity, and they have similar physicochemical properties. When Fe-Cu bimetals were introduced in the support (Fig. 8e and f), the reduction peaks of Cu oxide move slightly to a higher temperature, while the reduction peaks of Fe oxide move to a lower temperature. In addition, it produces some less reducible metal species (γ, γ₁ and γ₂) for Fe-Cu bimetallic supported samples. The H₂-TPR profiles show that Fe and Cu species have strong interaction.

As the catalytic reaction often depends on the diffusion of reactants and the physicochemical properties of the active centre, the phenol degradation was applied as a probe reaction to evaluate the influence of hollow structure and the Fe-Cu bimetallic effect. Fig. 9 shows the results of phenol degradation catalyzed by Fe containing zeolites. There are clear differences in the catalytic activity among them (Fig. 9A). To quantitatively compare the activities of these samples, the reaction rate constants (k) were calculated by adopting the pseudo first-order model (equation 2) typically used to describe catalytic degradation assuming a low initial concentration of pollutant [42].

$$\ln(C_0/C_t) = kt \quad (2)$$

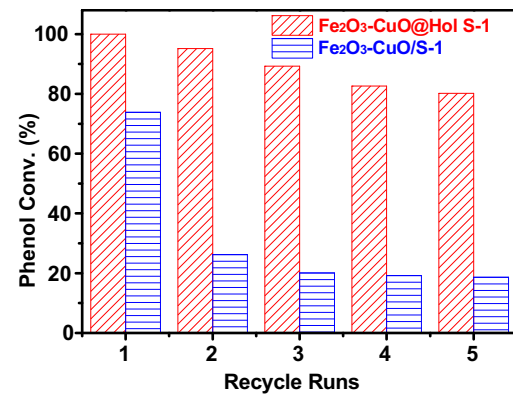


Fig. 10. The recycling performances of Fe₂O₃—CuO@Hol S-1 and Fe₂O₃—CuO/S-1.

Plots of ln(C₀/C_t) versus reaction time (t) are provided in Fig. 9B. The linear relationships point to each degradation following first-order kinetics. Apparent rate constants were determined to be 0.0028, 0.0210 and 0.0549 min⁻¹ for Fe₂O₃/S-1, Fe₂O₃@Hol S-1 and Fe₂O₃—CuO@Hol S-1, respectively, demonstrating the catalytic activity of the Fe₂O₃@Hol S-1 and Fe₂O₃—CuO@Hol S-1 to be about 7.5 and 20 times higher than that of Fe₂O₃/S-1, respectively. The link of the properties with the performance of different catalysts as below: (1) Compared to the metal oxide located in the micropores of the zeolite, the encapsulation of the metal oxide in a relatively open space facilitates the adsorption/activation of the reactant on the metal oxide surface. On the other hand, the short microporous channels (20 nm) of the hollow zeolite facilitate the diffusion of reactants and products. Therefore, encapsulated Fe and/or Fe-Cu show higher activity for phenol degradation (Fe₂O₃/S-1 vs. Fe₂O₃@Hol S-1 and Fe₂O₃—CuO/S-1 vs. Fe₂O₃—CuO@Hol S-1). (2)

Table 3

Metal leaching performance analysis by ICP.

Sample Code	Metal leaching	
	Fe (mg/L)	Cu (mg/L)
Fe ₂ O ₃ /S-1	1.86	—
Fe ₂ O ₃ @Hol S-1	0.44	—
Fe ₂ O ₃ —CuO/S-1	1.67	0.93
Fe ₂ O ₃ —CuO@Hol S-1	0.28	0.35

Hydroxyl radical (·OH), produced from H₂O₂ in the chain reaction initiated by Fe²⁺, is widely accepted as a strong oxidant for its high redox potential in Fenton system (Table S1). Our previous studies show that, the catalytic activity of bimetallic (Fe-Cu) catalyst was better than that of single-component Fe catalyst as the active component for the Fenton reaction. [30] The main reason is that the conversion of Fe³⁺ → Fe²⁺ to Fe³⁺ + Cu⁺ → Fe²⁺ + Cu²⁺ reduced the redox potential from 0.77 eV to 0.60 eV. In the present work, TEM, XRD, ⁵⁷Fe Mössbauer, H₂-TPR results confirm that the Fe-Cu particles show strong bimetallic interaction, leading to their higher activity for phenol degradation (Fe₂O₃/S-1 vs. Fe₂O₃—CuO/S-1 and Fe₂O₃@Hol S-1 vs. Fe₂O₃—CuO@Hol S-1). (3) Since the reaction occurs in the solid-liquid interface, increasing the surface area of the metal oxide will significantly enhance the catalyst activity, especially happens in the situation of metal oxide used as heterogeneous Fenton catalyst. In the present work, the encapsulated Fe-Cu catalysts exhibit the superior activity for phenol degradation due to their well dispersion (3.7 nm). The catalytic performance with phenol degradation rates and kinetic constants of the catalysts prepared using metal nitrates was shown in Fig. S1. The results show that the degradation rates of phenol were slower when the catalysts were prepared with metal nitrate. This is due to the poor dispersion of the metal prepared using the metal nitrate, which is consistent with the TEM results (Fig. 2).

More interestingly, the size of the encapsulated Fe₂O₃—CuO particles is larger than that of zeolite micropores, preventing the leaching of metal oxide (Table 3). From Fig. 10, we conclude that sample Fe₂O₃—CuO@Hol S-1 maintains 80% phenol conversion after 5 recycle runs. The Fe₂O₃—CuO@Hol S-1 catalyst after 5 recycle runs was checked by TEM (Fig. S2). It can be seen that, the Fe-Cu bimetallic oxide nanoparticles were still encapsulated inside the hollow zeolites with excellent dispersion after the reaction.

4. Conclusions

Fe-Cu binary metal oxide nanoparticles with a small average size of 3.7 nm have been successfully encapsulated in hollow Silicalite-1 single crystals. Whether the metal oxide particles can be encapsulated in the hollow zeolite also depends on the melting points of precursor salts because melting or softening during drying can lead to larger particle size. The large metal oxide particles easily fall down from the surface during the “dissolution-recrystallization” process and remain on the hollow crystal surfaces after TPAOH treatment. Compared with single metal oxides (Fe₂O₃ or CuO) in the hollow crystals, Fe₂O₃—CuO@Hol S-1 enhances the dispersion of Fe-Cu bimetallic oxide nanoparticles, and the interaction between Fe, Cu and support. These advantages make the catalyst highly active in the phenol degradation. In addition, the particle size of encapsulated Fe₂O₃—CuO is larger than that of zeolite micropores, preventing the leaching of metal oxide and thus greatly improves the catalyst reusability.

Acknowledgements

This work was supported by the State Key Laboratory of Fine Chemicals (KF1605), by the State Key Program of National Natu-

ral Science Foundation of China (Grant No. 21236008) and by the QianRen Type B Award to CS from Chinese government.

Appendix A. Supplementary data

Supplementary data associated with this article can be found, in the online version, at <http://dx.doi.org/10.1016/j.cattod.2017.02.001>.

Notes and references

- [1] M. Munoz, Z.M. de Pedro, J.A. Casas, J.J. Rodriguez, *Appl. Catal. B Environ.* 176–177 (2015) 249–265.
- [2] E. Brillas, E. Mur, R. Sauleda, *Appl. Catal. B Environ.* 16 (1998) 31–42.
- [3] E. Neyens, J. Baeyens, J. Hazard. Mater. B98 (2003) 33–50.
- [4] E. Brillas, I. Sires, M.A. Oturan, *Chem. Rev.* 109 (2009) 6570–6631.
- [5] J.J. Pignatello, E. Oliveros, A. Mackay, *Crit. Rev. Environ. Sci. Technol.* 36 (2006) 1–84.
- [6] O.P. Taras, S.A. Yashnik, A.B. Ayusheev, A.S. Piskun, R.V. Prihodko, Z.R. Ismagilov, V.V. Goncharuk, V.N. Parmon, *Appl. Catal. B Environ.* 140–141 (2013) 506–515.
- [7] M.B. Hocking, D.J. Intibar, *J. Chem. Technol. Biotechnol.* 35A (1985) 365–381.
- [8] K. Fajerwerg, H. Debellefontaine, *Appl. Catal. B Environ.* 10 (1996) L229–L235.
- [9] D.J. Martin, G. Liu, S.J.A. Moniz, Y. Bi, A.M. Beale, J. Ye, J. Tang, *Chem. Soc. Rev.* 44 (2015) 7808–7828.
- [10] K.A. Sashkina, V.S. Labko, N.A. Rudina, V.N. Parmon, E.V. Parkhomchuk, *J. Catal.* 299 (2013) 44–52.
- [11] Z. Cui, Z. Chen, C. Cao, L. Jiang, W. Song, *Chem. Commun.* 49 (2013) 2332–2334.
- [12] X. Li, X. Liu, L. Xu, Y. Wen, J. Ma, Z. Wu, *Appl. Catal. B Environ.* 165 (2015) 79–86.
- [13] P. Shukla, S. Wang, H. Sun, H. Ang, M. Tadé, *Chem. Eng. J.* 164 (2010) 255–260.
- [14] Y. Wang, H. Zhao, G. Zhao, *Appl. Catal. B Environ.* 164 (2015) 396–406.
- [15] M. Zhu, G. Diao, *J. Phys. Chem. C* 115 (2011) 18923–18934.
- [16] L. Hou, Q. Zhang, F. Jérôme, D. Duprez, H. Zhang, S. Royer, *Appl. Catal. B Environ.* 144 (2014) 739–749.
- [17] Y. Wang, H. Zhao, G. Zhao, *Appl. Catal. B Environ.* 164 (2015) 396–406.
- [18] R.C.C. Costa, M.D.F.F. Lelis, L.C.A. Oliveira, J.D. Fabris, J.D. Ardisson, R.R.V.A. Rios, C.N. Silva, R.M. Lago, *Catal. Commun.* 4 (2003) 525–529.
- [19] X. Li, J. Liu, A.I. Rykov, H. Han, C. Jin, X. Liu, J. Wang, *Appl. Catal. B Environ.* 179 (2015) 196–205.
- [20] X. Liang, Y. Zhong, S. Zhu, L. Ma, P. Yuan, J. Zhu, H. He, Z. Jiang, J. Hazard. Mater. 199–200 (2012) 247–254.
- [21] S. Yang, H. He, D. Wu, D. Chen, X. Liang, Z. Qin, M. Fan, J. Zhu, P. Yuan, *Appl. Catal. B Environ.* 89 (2009) 527–535.
- [22] F. Magalhães, M.C. Pereira, S.E.C. Botrel, J.D. Fabris, W.A. Macedo, R. Mendonça, R.M. Lago, L.C.A. Oliveira, *Appl. Catal. A Gen.* 332 (2007) 115–123.
- [23] A. Corma, *Chem. Rev.* 97 (1997) 2373–2419.
- [24] J. Mielby, J.O. Abildstrom, F. Wang, T. Kasama, C. Weidenthaler, S. Kegnaes, *Angew. Chem. Int. Ed.* 53 (2014) 12513–12516.
- [25] M. Choi, Z. Wu, E. Iglesia, *J. Am. Chem. Soc.* 132 (2010) 9129–9137.
- [26] B. Li, B. Sun, X. Qian, W. Li, Z. Wu, Z. Sun, M. Qiao, M. Duke, D. Zhao, *J. Am. Chem. Soc.* 135 (2013) 1181–1184.
- [27] D. Verboekend, R. Caicedo-Realpe, A. Bonilla, M. Santiago, J. Pérez-Ramírez, *Chem. Mater.* 22 (2010) 4679–4689.
- [28] M. Hartmann, *Angew. Chem. Int. Ed.* 43 (2004) 5880–5882.
- [29] C.H. Christensen, I. Schmidt, A. Carlsson, K. Johannsen, K. Herbst, *J. Am. Chem. Soc.* 127 (2005) 8098–8102.
- [30] L. Luo, C. Dai, A. Zhang, J. Wang, M. Liu, C. Song, X. Guo, *Catal. Sci. Technol.* 5 (2015) 3159–3165.
- [31] N. Ren, Y. Yang, Y. Zhang, Q. Wang, Y. Tang, *J. Catal.* 246 (2007) 215–222.
- [32] C. Dai, A. Zhang, L. Li, K. Hou, F. Ding, J. Li, D. Mu, C. Song, M. Liu, X. Guo, *Chem. Mater.* 25 (2013) 4197–4205.
- [33] S. Li, T. Boucheron, A. Tuel, D. Farrusseng, F. Meunier, *Chem. Commun.* 50 (2014) 1824–1826.
- [34] E. Özge Kerkez-Kuyumcu, K.F. Kibar Dayıoğlu, A.N. Gedik Akin, Özkara-Aydinoğlu, Şeyma, *J. Photochem. Photobiol. A* 311 (2015) 176–185.
- [35] W.J. Sun, J. Li, G.P. Yao, M. Jiang, F.X. Zhang, *Catal. Commun.* 16 (2011) 90–93.
- [36] Nadia Riaz, F.K. Chong, Binay K. Dutta, Zakaria B. Man, M. Saqib Khan, Ela Nurlaela, *Chem. Eng. J.* 185–186 (2012) 108–119.
- [37] R.M. Ramli, C.F. Kait, A.A. Omar, *Adv. Mater. Res.* 845 (2013) 421–425.
- [38] K. Woo, J. Hong, S. Choi, H. Lee, J. Ahn, C.S. Kim, S.W. Lee, *Chem. Mater.* 16 (2004) 2814–2818.
- [39] L. Luo, C. Dai, A. Zhang, J. Wang, M. Liu, C. Song, X. Guo, *RSC Adv.* 5 (2015) 29509–29512.
- [40] J. Sun, L. Zhang, C. Ge, C. Tang, L. Dong, *Chin. J. Chem.* 35 (2014) 1347–1358.
- [41] T. Zhang, J. Liu, D. Wang, Z. Zhao, Y. Wei, K. Cheng, G. Jiang, A. Duan, *Appl. Catal. B Environ.* 148–149 (2014) 520–531.
- [42] Y. Feng, L. Li, M. Ge, C. Guo, J. Wang, L. Liu, *ACS Appl. Mater. Interfaces* 2 (2010) 3134–3140.